Review of Scientific Instruments | ARTICLE | pubs.aip.org/aip/rsi

MilliKelvin microwave impedance microscopy in a dry dilution refrigerator

Cite as: Rev. Sci. Instrum. 94, 093705 (2023); doi: 10.1063/5.0159548
Submitted: 24 May 2023 • Accepted: 2 September 2023 •
Published Online: 29 September 2023

View Online

Export Citation

CrossMark

Leonard Weihao Cao, Chen Wu, Rajarshi Bhattacharyya, Ruolun Zhang, and Monica T. Allen[a)

AFFILIATIONS

Department of Physics, University of California, San Diego, California 92093, USA

[a)]Author to whom correspondence should be addressed: mtallen@physics.ucsd.edu

ABSTRACT

Microwave impedance microscopy (MIM) is a near-field imaging technique that has been used to visualize the local conductivity of materials with nanoscale resolution across the GHz regime. In recent years, MIM has shown great promise for the investigation of topological states of matter, correlated electronic states, and emergent phenomena in quantum materials. To explore these low-energy phenomena, many of which are only detectable in the milliKelvin regime, we have developed a novel low-temperature MIM incorporated into a dilution refrigerator. This setup, which consists of a tuning-fork-based atomic force microscope with microwave reflectometry capabilities, is capable of reaching temperatures down to 70 mK during imaging and magnetic fields up to 9 T. To test the performance of this microscope, we demonstrate microwave imaging of the conductivity contrast between graphite and silicon dioxide at cryogenic temperatures and discuss the resolution and noise observed in these results. We extend this methodology to visualize edge conduction in Dirac semi-metal cadmium arsenide in the quantum Hall regime.

Published under an exclusive license by AIP Publishing. https://doi.org/10.1063/5.0159548

03 October 2023 19:47:21

I. INTRODUCTION

Microwave imaging techniques have been developing rapidly over the past several decades and involve transmitting MHz to GHz microwave signals to sample surfaces through sharp-ended probes and collecting the microwave response. To date, there are several implementations of the scanning microwave microscope, such as sharp tips in coaxial resonators, microwave resonators on quartz tuning forks, and probes with impedance matching networks.[1–6] In this article, we focus on the specific implementation of microwave impedance microscopy (MIM), which has the capacity to probe the local conductivity and permittivity of quantum materials with nanoscale spatial resolution.[6–17] This enables direct visualization of the microscopic nature of electronic states, including the real-space disorder landscape, multi-domain behavior, or the presence of topological modes that propagate along the sample boundaries.[1,2,4,5,18,19] By coupling microwaves with a wavelength of 1–100 cm to a sharp metallic probe and collecting the reflected signal, MIM characterizes the complex admittance between the tip and the sample without the requirement for the sample to be conductive, which is less restrictive than other electronic imaging techniques.[20–24] As demonstrated in recent experiments, MIM can provide insight into the real-space nature of correlated states and topological states in two-dimensional heterostructures.[16,17,25–29] However, many of these states are characterized by low energy scales and are, therefore, most robust at milliKelvin temperatures, motivating the development of cryogenic MIM instrumentation. Thus far, most state-of-the-art near-field microwave imaging has been performed in 1.5–2 K[30] or He-3 cryostats, which can reach a minimum temperature of 300–450 mK.[3,29]

Here, we report on the construction of a novel milliKelvin MIM, which will support spatially resolved detection of quantum electronic states at ultra-low temperatures. This setup consists of a scanning probe microscope with tuning-fork-based height feedback integrated into a dry dilution refrigerator. A sharp metallic probe driven by an AC signal at microwave frequency is coupled to the tuning fork and scanned over the sample. Using reflectometry, MIM detects the sample's response to high frequency electromagnetic fields emanating from the probe.

To demonstrate the measurement capabilities of this setup, we present MIM images of the conductivity contrast between graphite and SiO_2 down to temperatures of 70 mK. Finally, we also

demonstrate microwave imaging of topological edge states in Cd_3As_2 thin films in the quantum Hall regime at the base temperature.

II. EXPERIMENTAL SETUP

This setup consists of a custom-designed tuning fork based atomic force microscope (AFM) integrated into a Leiden Cryogenics CF-CS110 dilution refrigerator. The microscope housing is in thermal equilibrium with the mixing chamber plate on the cold-insertable probe, which is loaded into a dilution refrigerator, as shown schematically in Fig. 1(a). Figure 1(b) shows the design of the microscope head, which houses an etched tungsten wire mounted onto the end of one prong of a tuning fork (TF) mechanical resonator (blue box).[31] The oscillation amplitude of the TF is monitored for continuous height feedback, which enables tapping-mode topographic imaging.[32] Below the tip holder, the sample stage is mounted on a stack of CuBe piezoelectric scanners (Attocube AN-Sxyz100) and positioners [ANPx(z)100], which control fine xyz scanning (up to $40 \times 40\ \mu m^2$ below 4 K) and coarse positioning ($5 \times 5\ mm^2$ below 4 K), respectively.

On the MIM circuitry side, GHz signals are generated by an analog signal generator, and one split branch of the signal is coupled to the tip via an impedance matching network (IMN),[33] which is responsible for minimizing the reflected signal [inset in Fig. 1(c)].[34] Unless otherwise mentioned, measurements in the article are performed with 0 dBm source power, and the power reaching the tip is −33 dBm. A plot of the reflected microwave power S_{11} of an example IMN is shown in Fig. 1(c), showing the first resonance at 1.8 GHz. The reflected signal from the tip passes through two directional couplers mounted on the probe-still plate (1 K) to cancel out the residual reflected power.

The signal from the sample is then amplified by a cryogenic amplifier (Cosmic Microwave Technology CITCRYO1-12) mounted on the 3 K stage, after which the signal propagates out of the probe and gets further amplified and demodulated at room temperature, as shown in Fig. 1(a).

During the tip approach procedure, active height feedback can be performed by monitoring either the TF oscillation amplitude or the MIM signal. Here, we use a Nanonis SC5 controller to excite and track the TF oscillation and control the fine scanners during imaging.[34] Figure 1(d) displays a measurement of the oscillation amplitude of the tuning fork as a function of excitation frequency, showing the resonance peak near 32.768 kHz. The Q-factor of the

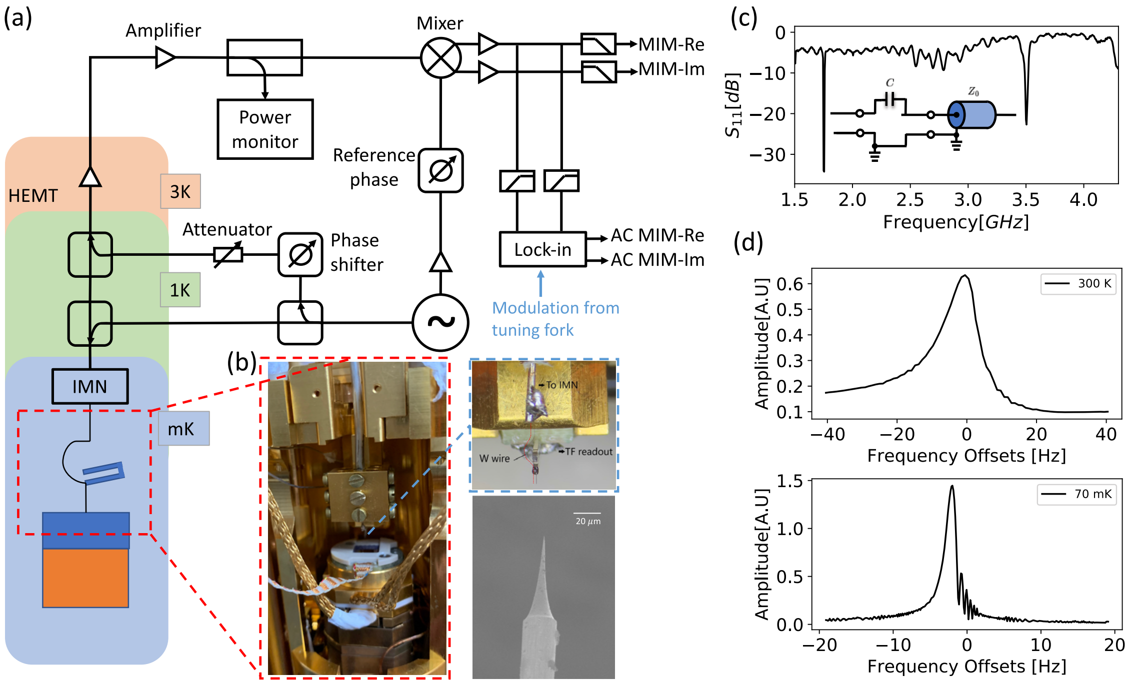

FIG. 1. Scanning probe microscopy system with combined AFM and MIM readout integrated into a dilution refrigerator. (a) Schematic of the scanning MIM readout electronics and hardware integrated into a dilution refrigerator. The shaded regions refer to the different thermal stages inside the fridge. (b) *Left panel*: Photograph of the microscope head, scanners, and sample stage (corresponding to the red box in the schematic). *Right panels*: Zoomed-in side view of the gold-coated tungsten tip glued onto one prong of the tuning fork and soldered to the end of the IMN on the other end. The back of the TF is electrically connected for oscillation readout (blue box); scanning electron microscope image of the etched tungsten tip used for combined AFM and MIM imaging. (c) Plot of the reflect microwave power S_{11} of the impedance matching network (IMN) shows the fundamental resonance at 1.8 GHz. *Inset*: Circuit diagram of the IMN with a 0.2 pF capacitor and 5 cm of coax connected in series. (d) Plots of the oscillation amplitude of the tuning fork as a function of frequency, showing the mechanical resonance used for height feedback. The upper and lower panels show the resonance peak at room temperature and 70 mK, respectively.

03 October 2023 19:47:21

Published under an exclusive license by AIP Publishing

resonance is around 500–2000 at room temperature (upper panel), while at base temperature, it can easily reach 10 000–100 000 (lower panel).

The main technical challenge of microwave imaging in a dry dilution fridge is the emergence of new noise sources, which impact both spatial resolution and the signal-to-noise ratio of the microwave reflectometry measurements. There are two main sources of increased noise: (1) mechanical pulse tube vibrations, which are associated with the cooling mechanism of the dilution fridge, place limits on the lateral spatial resolution and add noise to the measured MIM signal; and (2) the high Q factor of the tuning fork at mK temperatures leads to fluctuations in the tip–sample distance, which also couples with the pulse tube vibration. Our fridge is equipped with a pulse tube cryocooler operating at ~ 1.4 Hz,[35,36] generating vibrations that amplitude modulate the tuning fork oscillation and consequently also modulate the GHz MIM signal. To mitigate these vibrations, we physically decoupled the pulse tube motion from the microscope by unscrewing the rotary valve from the fridge and putting isolation foam in between,[37] while the high-pressure helium lines connected to the compressor are wrapped with acoustic pipe lagging. On the other hand, the high Q factor can be reduced by further breaking the symmetry of the two prongs, and two methods we have been using include adding extra glue during the tip-gluing process and balancing the strain from the tip to the TF.

We found that performing AC-mode MIM imaging, as described below, largely eliminates background oscillations in the images that arise from pulse tube vibrations. In AC height-modulated imaging mode, a low frequency lock-in amplifier (SR830) is added to the output of the GHz frequency mixer to demodulate the reflected MIM signal at the tuning fork resonance frequency (32 kHz), after which low-pass filters can be used to attenuate noise.[34] We note that because the GHz MIM signal (from the tip) is amplitude-modulated by both the tuning fork oscillation at 32 kHz and the pulse tube vibration, there are multiple side-bands around the measurement frequency. Therefore, voltage preamplifiers with band-pass filters between 10 and 30 kHz (SR560, 6 dB/oct) are added to the output of the GHz mixer to both filter out the DC-MIM signal, which would overload the lock-in amplifier, amplify the signal amplitude, and reduce the out-of-band noise, after which the MIM signal is fed into the SR830 lock-in amplifier for demodulation. During this step, the lock-in amplifier multiplies the MIM input signal with a TF reference signal (provided by the measured piezo current from the tuning fork, after amplification by a commercial low-noise charge amplifier) to extract the in-phase components. Both the filters inside SR830 and the additional low-pass filters (SR560, 1 Hz low-pass) added to the output of the lock-in are chosen to eliminate noise at the pulse tube vibration frequency.

III. RESULTS AND DISCUSSION

We characterized the low temperature performance of the AFM on a sample consisting of an array of etched SiO_2 holes patterned on a Si wafer, as depicted in the optical image in Fig. 2(a). Cryogenic AFM measurements are used to visualize the topographic profile of a $5 \times 5\ \mu m^2$ scan region at 70 mK, as depicted in Fig. 2(b). Figure 2(c) shows a cross-sectional cut of this AFM image, whose position is marked by the black line, revealing a noise level of roughly 3 nm. To more carefully assess the magnitude of the z-noise during AFM scanning, we performed 96 × 96-pixel noise scans over a $1 \times 1\ nm^2$ area, such that the spatial profile is irrelevant. Root mean square (rms) roughness was calculated using Gwyddion after line fitting, which gives z-noise levels in the range of 1.8–2.2 nm. Furthermore, upon careful inspection of Fig. 2(b), we noticed that a tilted stripe pattern appears as a background modulation in the AFM image. By taking a Fourier transform of these data, we found that the stripe pattern has a frequency of 1.4 Hz, which coincides with the frequency of the pulse tube.

Next, to demonstrate our combined AFM and MIM imaging capabilities at low temperatures, we measured the spatial contrast of

03 October 2023 19:47:21

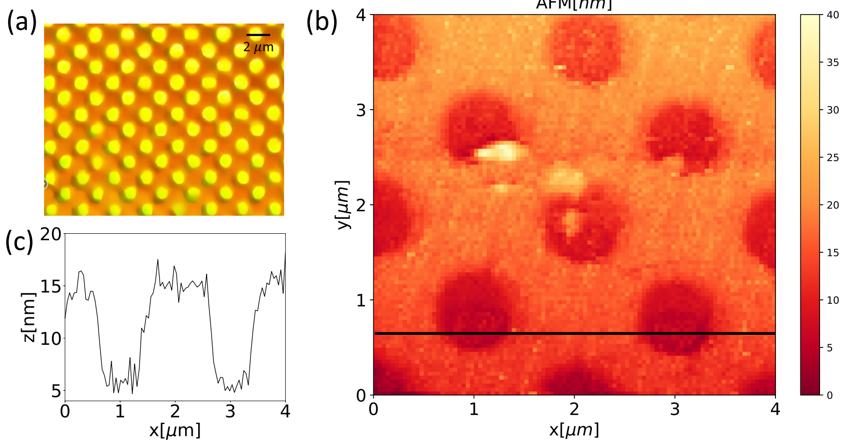

FIG. 2. Topographic imaging of a micropatterned dielectric film at mK temperatures using tuning-fork-based atomic force microscopy. (a) Optical image of an etched array of holes in SiO_2. The diameter and spacing of the holes are 1 μm. The hole depth is 20 nm. (b) AFM spatial scan at 70 mK. The scan covers $4\times 4\ \mu m^2$, and the scan speed is 400 nm s^{-1}. (c) Cross-sectional line cut corresponding to the black line in (b).

Published under an exclusive license by AIP Publishing

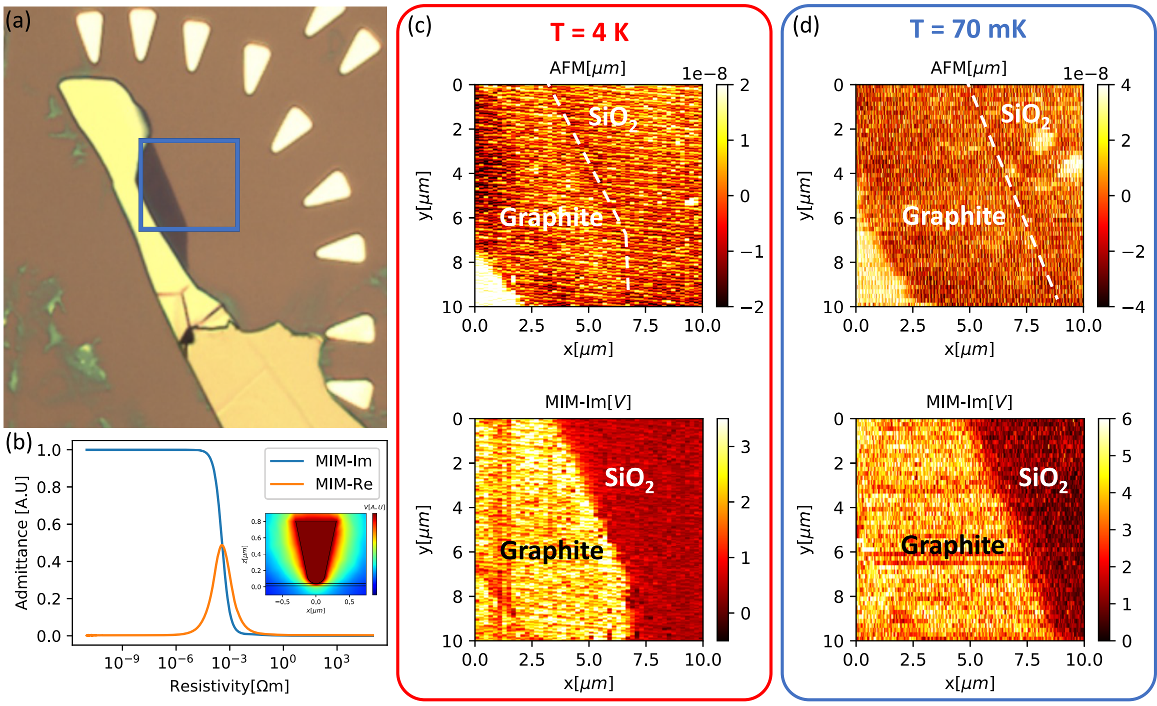

FIG. 3. Microwave impedance microscopy of graphite at milliKelvin temperatures. (a) Optical image of a graphite flake exfoliated onto a SiO_2/Si substrate. The dark purple region has a thickness of 3–5 nm, and the light yellow region has a thickness of ~ 20 nm. The blue box marks the imaging window for (c) and (d). (b) Theoretical MIM response curves simulated at 1.8 GHz, illustrating the evolution of the MIM contrast with the sample conductivity. *Inset*: vertical cut of the potential distribution for the tip–sample interaction, calculated using finite-element analysis. (c) AFM and MIM imaging of the graphite flake at 4 K, with the scan window covering the 20 nm region (lower left), 3–5 nm region (middle), and the SiO_2 region (upper right). The scan speed is 0.5 μm/s. (d) AFM and MIM images of the same location at 70 mK. The scan speed is 0.2 μm/s.

03 October 2023 19:47:21

the MIM response across the boundary between graphite and SiO_2 at 70 mK. Figure 3(a) shows an optical image of the graphite sample, which has terraces of varying thicknesses: the purple region is ~ 3 nm and the bright yellow region is 15–20 nm.

In Fig. 3, panels (c) and (d) display AFM and MIM images of the graphite/SiO_2 interface measured at 4 K and 70 mK, respectively. In both sets of AFM images, the 3/20 nm step height in graphite is clearly visible, while the graphite/SiO_2 boundary only shows a faint contour as the z-movement of the scanner to compensate for fluctuations in the tip–sample distance dominates over the 3 nm boundary. Meanwhile, we observe a sharp contrast in the MIM signal across the graphite/SiO_2 boundary due to the different conductivities of the two materials, as predicted by the response curves in Fig. 3(b). To explain the experimental observations, one can model the tip–sample interaction for this system using finite element analysis.[28] In the numerical simulation, the tip is defined to be 1 V, and the bottom of the SiO_2 is set at 0 V, the ground. The side of the sample is electrically floating. For a sample with scalar conductivity, the simulation can be used to calculate the MIM response curves as a function of sample resistivity, which should be expected to have a response curve similar to the lump-circuit model defined for MIM imaging.[17,38] For a better discussion of the lump-circuit model, readers can refer to the supplementary material. At a measurement frequency of 1.8 GHz, the imaginary part of the MIM response should monotonically decrease with the sample resistivity, saturating when the resistivity is higher than 10^{-2} $\Omega \cdot$ m (insulating limit) or lower than 10^{-5} $\Omega \cdot$ m (conductive limit), as shown in Fig. 3(b). A cross-sectional profile of the penetration of the tip potential into the sample is provided in the inset. Based on our observations in the imaging, we estimate the MIM spatial resolution to be below 200 nm, constrained by the apex geometry of the etched tungsten tip and mechanical noise from pulse tube vibrations.

We also apply this methodology to visualize edge states at the boundaries of thin film cadmium arsenide (Cd_3As_2), a novel three-dimensional Dirac semi-metal, in the quantum Hall regime.[39,40] A cross-sectional schematic of the epitaxially grown heterostructure is shown in Fig. 4(a), where the film thickness is 20 nm.[41,42] The Cd_3As_2 device is lithographically patterned and etched into strips of width 10–15 μm, which are electrically grounded. Transport measurements were performed to characterize the magnetic field behavior of the sample, which revealed dips in the longitudinal resistance at around 4.7 and 6.5 T, as shown in Fig. 4(b). These minima should correspond to the emergence of quantum Hall plateaus.[43]

To shed light on the real-space conductivity profile of Cd_3As_2 in the quantum Hall regime and monitor its evolution across the topological phase transition between plateaus, MIM measurements

Published under an exclusive license by AIP Publishing

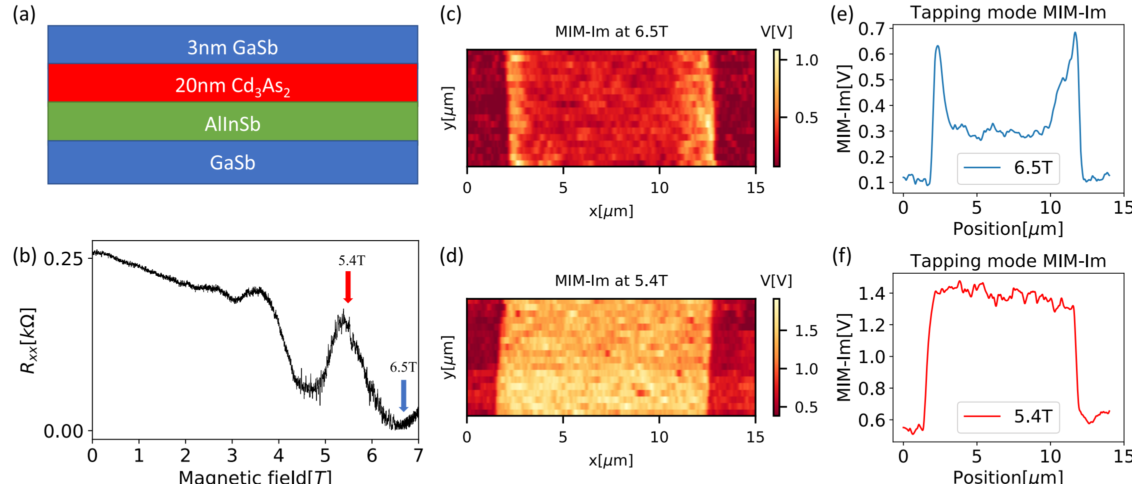

FIG. 4. Microwave imaging of edge modes in a cadmium arsenide film in the quantum Hall regime. (a) Cross-sectional schematic of an epitaxially grown Cd_3As_2 heterostructure. (b) Transport measurement of the longitudinal resistance R_{xx} as a function of the magnetic field at 90 mK. The minima correspond to the emergence of quantum Hall plateaus. (c) MIM image at 6.5 T, revealing a sharp enhancement of the reflected signal at the boundaries of a quantum Hall insulator state. (d) MIM image at 5.4 T, showing spatially uniform conductivity at the transition between quantum Hall plateaus (e)–(f) Cross-sectional line cuts of the MIM response across the sample extracted from (c) and (d), respectively.

were performed at a series of magnetic fields at a base temperature of 90 mK. Microwave imaging reveals a sharp enhancement of the reflected MIM signal at the boundaries of the sample in the quantum Hall insulator state, which rapidly decays into the bulk of the sample, as shown in Fig. 4(c). Meanwhile, we observed a spatially uniform conductivity at the transition between quantum Hall plateaus when the longitudinal resistance deviates from zero at B = 5.4 T [Fig. 4(d)]. The variation of the MIM signal between different lines comes both from the noise in the MIM signal and from spatial inhomogeneities in the sample.

To more clearly compare the spatial dependence of the MIM signal in these two regimes, in Figs. 4(e) and 4(f), we plot the cross-sectional profiles of the MIM response across the sample extracted from panels (c) and (d), respectively. These low temperature microwave images reveal sharply enhanced edge conduction that encloses an insulating interior in the quantum Hall regime, which is consistent with the results of transport measurements performed on this system in prior experimental studies.

We note that one way to improve signal quality is to use "floating" AC-mode MIM, where imaging is performed with the tip retracted a fixed distance (60–100 nm) above the sample surface. At this distance, the AFM channel will not be modulated due to the topography feedback, but the MIM tip can still interact with the sample via the electromagnetic fields in the vicinity of the tip (when operated in the near-field regime). Because periodic oscillations in the tip–sample distance at the tuning fork resonance are decoupled from the surface roughness of the sample, noise in the MIM response can be dramatically reduced in floating mode. Figure 5 shows the results of a floating mode MIM scan performed at 3 GHz and T = 70 mK, with the tip lifted 100 nm above an hBN-covered graphite layer. The tip apex is around 0.8 μm, which is reflected in the spatial profile of the MIM signal change across the boundary

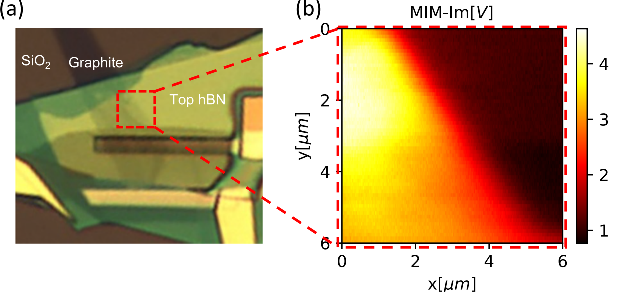

FIG. 5. Demonstration of low-noise height-modulated MIM in a dry dilution fridge. (a) Optical image of a van der Waals heterostructure with a graphite flake (around 5 nm thick) covered by hBN (around 50 nm thick). From the bottom up, the whole stack is graphite (5 nm, connected from the leftmost gold contact), bottom hBN (30 nm, dark green), graphite contact (5–10 nm, middle), and top hBN (50 nm, bright green). The imaging window has 30 nm hBN, 5–10 nm graphite, and 50 nm hBN from the bottom up. (b) A floating mode MIM image of the region enclosed by the red square in panel (a), acquired at 70 mK. The measurement frequency is 3 GHz, and the tip is retracted 100 nm from the highest feature inside the scan window.

between the graphite flake and hBN. In this case, the signal-to-noise ratio is even better than that observed in tapping mode MIM images [Figs. 3(c) and 3(d)], which is especially useful for fixed-location MIM measurements. However, this advantage comes at the expense of signal size, as the tip is further away from the sample than in tapping mode. The varying MIM signal in the graphite region is due to the fact that during a floating scan, the tip is hovering at a fixed absolute z-position while the sample has a surface tilt, which means the tip–sample distance is varying in the whole frame. We estimate the

03 October 2023 19:47:21

Published under an exclusive license by AIP Publishing

distance to be around 70 nm in the upper-left corner and 100 nm in the lower-right corner.

The choice of tip–sample distance for floating-mode measurements is a compromise between maximizing signal sensitivity and minimizing the risk of a tip crash due to vertical fluctuations in the tip–sample distance, which arise from pulse tube vibrations and are aggravated by the large Q factor of the tuning fork at mK temperatures. For larger scan windows or rougher sample surfaces, the tip may need to be retracted further. We expect the sensitivity of floating mode to be around $0.01 - 0.1\text{aF}/\sqrt{\text{Hz}}$ at 0.1 μW input power, and in our case, the noise is mostly due to vertical modulations of the tip–sample distance.[25]

IV. CONCLUSION AND OUTLOOK

In summary, we report on the development of a microwave impedance microscope that operates at temperatures down to 70 mK. This is achieved by incorporating a TF-based AFM with near-field GHz imaging capabilities into a dry dilution refrigerator.

Pushing the limits of MIM into new low temperature regimes should enable local sensing of quantum phenomena that only exist at low energy scales, including certain topological states of matter, domain wall physics at phase transitions, quantum states arising from geometric confinement in mesoscopic devices, and correlated states in two-dimensional materials and van der Waals heterostructures. Because this instrumentation is equipped with combined transport and imaging capabilities, it can also illuminate the correspondence between macroscopic transport behavior and the underlying microscopic nature of electronic states, including the real-space disorder landscape or the presence of edge modes.

During the preparation of this article, we became aware of an article on a related topic.[44] We are using the same tuning-fork based MIM circuitry, and in this article, we focus our efforts on mitigating the relevant AFM and MIM noise caused by the fluctuation in the tip–sample distance. The z-resolution of AFM in the reference is in the order of 0.1–0.3 nm, while in our case, it is 3–20 nm. The MIM sensitivity in the reference is mainly limited by the MIM setup, while our MIM sensitivity is constrained by the vertical tip–sample variation.

SUPPLEMENTARY MATERIAL

The supplementary material includes more information on the analysis of the pulse tube vibration frequency, a description of the lumped element model of MIM, and the determination of the MIM spatial resolution.

ACKNOWLEDGMENTS

We acknowledge Alex Lygo and Susanne Stemmer for providing cadmium arsenide devices for these experiments, Yongtao Cui for inspiring discussions, and Evan Cobb for helping develop some of the MIM circuitry. We gratefully acknowledge funding support from the UC Office of the President, specifically the UC Laboratory Fees Research Program (Award No. LFR-20-653926), the AFOSR Young Investigator Program (Award No. FA9550-20-1-0035), and the AFOSR/ARO MURI Program (Award No. FA9550-22-1-0270). This work was performed, in part, at the San Diego Nanotechnology Infrastructure (SDNI) of UCSD, a member of the National Nanotechnology Coordinated Infrastructure, which is supported by the National Science Foundation (Grant No. ECCS-2025752).

AUTHOR DECLARATIONS

Conflict of Interest

The authors have no conflicts to disclose.

Author Contributions

Leonard Weihao Cao: Data curation (lead); Formal analysis (equal); Methodology (equal); Software (lead); Visualization (supporting); Writing – original draft (lead); Writing – review & editing (equal). **Chen Wu**: Data curation (supporting); Formal analysis (equal); Methodology (equal); Visualization (lead); Writing – original draft (supporting); Writing – review & editing (equal). **Rajarshi Bhattacharyya**: Data curation (supporting); Methodology (equal); Writing – review & editing (supporting). **Ruolun Zhang**: Methodology (equal); Writing – review & editing (supporting). **Monica T. Allen**: Conceptualization (lead); Formal analysis (supporting); Funding acquisition (lead); Investigation (supporting); Methodology (supporting); Project administration (lead); Resources (lead); Supervision (lead); Writing – original draft (supporting); Writing – review & editing (equal).

DATA AVAILABILITY

The data that support the findings of this study are available from the corresponding author upon reasonable request.

REFERENCES

[1] I. Takeuchi, T. Wei, F. Duewer, Y. K. Yoo, X.-D. Xiang, V. Talyansky, S. P. Pai, G. J. Chen, and T. Venkatesan, "Low temperature scanning-tip microwave near-field microscopy of $YBa_2Cu_3O_{7-x}$ films," Appl. Phys. Lett. **71**, 2026–2028 (1997).

[2] S.-C. Lee, S.-Y. Lee, and S. M. Anlage, "Microwave nonlinearities of an isolated long $YBa_2Cu_3O_{7-\delta}$ bicrystal grain boundary," Phys. Rev. B **72**, 024527 (2005).

[3] S. E. de Graaf, A. V. Danilov, A. Adamyan, and S. E. Kubatkin, "A near-field scanning microwave microscope based on a superconducting resonator for low power measurements," Rev. Sci. Instrum. **84**, 023706 (2013).

[4] S. de Graaf, A. Danilov, and S. Kubatkin, "Coherent interaction with two-level fluctuators using near field scanning microwave microscopy," Sci. Rep. **5**, 17176 (2015).

[5] S. Geaney, D. Cox, T. Hönigl-Decrinis, R. Shaikhaidarov, S. Kubatkin, T. Lindström, A. Danilov, and S. de Graaf, "Near-field scanning microwave microscopy in the single photon regime," Sci. Rep. **9**, 12539 (2019).

[6] K. Lai, M. Ji, N. Leindecker, M. Kelly, and Z. Shen, "Atomic-force-microscope-compatible near-field scanning microwave microscope with separated excitation and sensing probes," Rev. Sci. Instrum. **78**, 063702 (2007).

[7] B. T. Rosner and D. W. van der Weide, "High-frequency near-field microscopy," Rev. Sci. Instrum. **73**, 2505–2525 (2002).

[8] H. P. Huber, M. Moertelmaier, T. M. Wallis, C.-J. Chiang, M. Hochleitner, A. Imtiaz, Y. J. Oh, K. Schilcher, M. Dieudonne, J. Smoliner, P. Hinterdorfer, S. J. Rosner, H. Tanbakuchi, P. Kabos, and F. Kienberger, "Calibrated nanoscale capacitance measurements using a scanning microwave microscope," Rev. Sci. Instrum. **81**, 113701 (2010).

03 October 2023 19:47:21

Published under an exclusive license by AIP Publishing

[9] K. Lai, W. Kundhikanjana, M. A. Kelly, and Z. X. Shen, "Nanoscale microwave microscopy using shielded cantilever probes," Appl. Nanosci. **1**, 13–18 (2011).

[10] K. Lai, W. Kundhikanjana, M. A. Kelly, Z.-X. Shen, J. Shabani, and M. Shayegan, "Imaging of Coulomb-driven quantum hall edge states," Phys. Rev. Lett. **107**, 176809 (2011).

[11] W. Kundhikanjana, Y. Yang, Q. Tanga, K. Zhang, K. Lai, Y. Ma, M. Kelly, X. Li, and Z. Shen, "Unexpected surface implanted layer in static random access memory devices observed by microwave impedance microscope," Semicond. Sci. Technol. **28**, 025010 (2013).

[12] E. Y. Ma, M. R. Calvo, J. Wang, B. Lian, M. Mühlbauer, C. Brüne, Y.-T. Cui, K. Lai, W. Kundhikanjana, Y. Yang, M. Baenninger, M. König, C. Ames, H. Buhmann, P. Leubner, L. W. Molenkamp, S. C. Zhang, D. Goldhaber-Gordon, M. A. Kelly, and Z. X. Shen, "Unexpected edge conduction in mercury telluride quantum wells under broken time-reversal symmetry," Nat. Commun. **6**, 7252 (2015).

[13] E. Y. Ma, Y.-T. Cui, K. Ueda, S. Tang, K. Chen, N. Tamura, P. M. Wu, J. Fujioka, Y. Tokura, and Z.-X. Shen, "Mobile metallic domain walls in an all-in-all-out magnetic insulator," Science **350**, 538–541 (2015).

[14] Y. Liu, C. Tan, H. Chou, A. Nayak, D. Wu, R. Ghosh, H.-Y. Chang, Y. Hao, X. Wang, J.-S. Kim, R. Piner, R. S. Ruoff, D. Akinwande, and K. Lai, "Thermal oxidation of WSe_2 nanosheets adhered on SiO_2/Si substrates," Nano Lett. **15**, 4979–4984 (2015).

[15] E. Seabron, S. MacLaren, X. Xie, S. V. Rotkin, J. A. Rogers, and W. L. Wilson, "Scanning probe microwave reflectivity of aligned single-walled carbon nanotubes: Imaging of electronic structure and quantum behavior at the nanoscale," ACS Nano **10**, 360–368 (2016).

[16] Z. Chu, E. C. Regan, X. Ma, D. Wang, Z. Xu, M. I. B. Utama, K. Yumigeta, M. Blei, K. Watanabe, T. Taniguchi, S. Tongay, F. Wang, and K. Lai, "Nanoscale conductivity imaging of correlated electronic states in WSe_2/WS_2 moiré superlattices," Phys. Rev. Lett. **125**, 186803 (2020).

[17] M. E. Barber, E. Y. Ma, and Z.-X. Shen, "Microwave impedance microscopy and its application to quantum materials," Nat. Rev. Phys. **4**, 61–74 (2022).

[18] S.-C. Lee and S. M. Anlage, "Spatially-resolved nonlinearity measurements of $YBa_2Cu_3O_{7-\delta}$ bicrystal grain boundaries," Appl. Phys. Lett. **82**, 1893–1895 (2003).

[19] T. Tai, B. G. Ghamsari, T. R. Bieler, T. Tan, X. X. Xi, and S. M. Anlage, "Near-field microwave magnetic nanoscopy of superconducting radio frequency cavity materials," Appl. Phys. Lett. **104**, 232603 (2014).

[20] M. Eriksson, R. Beck, M. Topinka, J. Katine, R. Westervelt, K. Campman, and A. Gossard, "Cryogenic scanning probe characterization of semiconductor nanostructures," Appl. Phys. Lett. **69**, 671–673 (1996).

[21] J. Döring, L. M. Eng, and S. C. Kehr, "Low-temperature piezoresponse force microscopy on barium titanate," J. Appl. Phys. **120**, 084103 (2016).

[22] C.-I. Lu, C. J. Butler, J.-K. Huang, Y.-H. Chu, H.-H. Yang, C.-M. Wei, L.-J. Li, and M.-T. Lin, "Moiré-related in-gap states in a twisted MoS_2/graphite heterojunction," Npj 2D Mater. Appl. **1**, 24 (2017).

[23] L. McGilly, A. Kerelsky, N. Finney, K. Shapovalov, E.-M. Shih, A. Ghiotto, Y. Zeng, S. Moore, W. Wu, Y. Bai *et al.*, "Seeing moiré superlattices," arXiv:1912.06629 (2019).

[24] M. R. Rosenberger, H.-J. Chuang, M. Phillips, V. P. Oleshko, K. M. McCreary, S. V. Sivaram, C. S. Hellberg, and B. T. Jonker, "Twist angle-dependent atomic reconstruction and moiré patterns in transition metal dichalcogenide heterostructures," ACS Nano **14**, 4550–4558 (2020).

[25] K. Lai, W. Kundhikanjana, M. Kelly, and Z. X. Shen, "Modeling and characterization of a cantilever-based near-field scanning microwave impedance microscope," Rev. Sci. Instrum. **79**, 063703 (2008).

[26] K. Lai, M. Nakamura, W. Kundhikanjana, M. Kawasaki, Y. Tokura, M. A. Kelly, and Z.-X. Shen, "Mesoscopic percolating resistance network in a strained manganite thin film," Science **329**, 190–193 (2010).

[27] E. Y. Ma, B. Bryant, Y. Tokunaga, G. Aeppli, Y. Tokura, and Z.-X. Shen, "Charge-order domain walls with enhanced conductivity in a layered manganite," Nat. Commun. **6**, 7595 (2015).

[28] X. Wu, Z. Hao, D. Wu, L. Zheng, Z. Jiang, V. Ganesan, Y. Wang, and K. Lai, "Quantitative measurements of nanoscale permittivity and conductivity using tuning-fork-based microwave impedance microscopy," Rev. Sci. Instrum. **89**, 043704 (2018).

[29] M. Allen, Y. Cui, E. Yue Ma, M. Mogi, M. Kawamura, I. C. Fulga, D. Goldhaber-Gordon, Y. Tokura, and Z.-X. Shen, "Visualization of an axion insulating state at the transition between 2 chiral quantum anomalous hall states," Proc. Natl. Acad. Sci. **116**, 14511–14515 (2019).

[30] W. Kundhikanjana, K. Lai, M. A. Kelly, and Z.-X. Shen, "Cryogenic microwave imaging of metal–insulator transition in doped silicon," Rev. Sci. Instrum. **82**, 033705 (2011).

[31] Y. Khan, H. Al-Falih, Y. Zhang, T. K. Ng, and B. S. Ooi, "Two-step controllable electrochemical etching of tungsten scanning probe microscopy tips," Rev. Sci. Instrum. **83**, 063708 (2012).

[32] H. Edwards, L. Taylor, W. Duncan, and A. J. Melmed, "Fast, high-resolution atomic force microscopy using a quartz tuning fork as actuator and sensor," J. Appl. Phys. **82**, 980–984 (1997).

[33] D. M. Pozar, *Microwave Engineering* (John Wiley & Sons, 2011).

[34] Y.-T. Cui, E. Y. Ma, and Z.-X. Shen, "Quartz tuning fork based microwave impedance microscopy," Rev. Sci. Instrum. **87**, 063711 (2016).

[35] C. Wang and P. Gifford, Development of 4 K pulse tube at cryomech, AIP Conf. Proc. **613**, 641–648 (2002).

[36] A. Chijioke and J. Lawall, "Vibration spectrum of a pulse-tube cryostat from 1Hz to 20 KHz," Cryogenics **50**, 266–270 (2010).

[37] R. Li, Y. Ikushima, T. Koyama, T. Tomaru, T. Suzuki, T. Haruyama, T. Shintomi, and A. Yamamoto, "Vibration-free pulse tube cryocooler system for gravitational wave detectors, Part II: Cooling performance and vibration, in *Cryocoolers 13* (Springer, 2005), pp. 703–710.

[38] T. Wang, C. Wu, M. Mogi, M. Kawamura, Y. Tokura, Z.-X. Shen, Y.-Z. You, and M. T. Allen, "Theory of the microwave impedance microscopy of Chern insulators," arXiv:2304.09227 (2023).

[39] R. Sankar, M. Neupane, S.-Y. Xu, C. Butler, I. Zeljkovic, I. Panneer Muthuselvam, F.-T. Huang, S.-T. Guo, S. K. Karna, M.-W. Chu, W. L. Lee, M. T. Lin, R. Jayavel, V. Madhavan, M. Z. Hasan, and F. C. Chou, "Large single crystal growth, transport property and spectroscopic characterizations of three-dimensional Dirac semimetal Cd_3As_2," Sci. Rep. **5**, 12966 (2015).

[40] T. Schumann, M. Goyal, H. Kim, and S. Stemmer, "Molecular beam epitaxy of Cd_3As_2 on a III-V substrate," APL Mater. **4**, 126110 (2016).

[41] M. Goyal, L. Galletti, S. Salmani-Rezaie, T. Schumann, D. A. Kealhofer, and S. Stemmer, "Thickness dependence of the quantum hall effect in films of the three-dimensional Dirac semimetal Cd_3As_2," APL Mater. **6**, 026105 (2018).

[42] A. C. Lygo, B. Guo, A. Rashidi, V. Huang, P. Cuadros-Romero, and S. Stemmer, "Two-dimensional topological insulator state in cadmium arsenide thin films," Phys. Rev. Lett. **130**(4), 046201 (2023).

[43] B. Guo, A. C. Lygo, X. Dai, and S. Stemmer, "$\nu = 0$ quantum hall state in a cadmium arsenide thin film," APL Mater. **10**, 091116 (2022).

[44] Z. Jiang, S. K. Chong, P. Zhang, P. Deng, S. Chu, S. Jahanbani, K. L. Wang, and K. Lai, "Implementing microwave impedance microscopy in a dilution refrigerator," Rev. Sci. Instrum. **94**, 053701 (2023).

03 October 2023 19:47:21

Published under an exclusive license by AIP Publishing